Nanoscale

PAPER

View Article Online
View Journal | View Issue

Cite this: *Nanoscale*, 2024, **16**, 15148

Design and fabrication of intermetallic NiCo electrocatalysts for the alkaline HER†

Chun Wu, *[a,b,c,d] Xuhui Wang,[a,b] Mengyao Huang,[a,b] Chao Meng,[a,b] Ling Chang,[c] Dake Xu [c] and Wenli Pei *[c]

Received 19th June 2024,
Accepted 23rd July 2024

DOI: 10.1039/d4nr02519a

rsc.li/nanoscale

The design and fabrication of highly efficient electrocatalysts are crucial for reducing energy consumption, improving hydrogen production rates, and prolonging the service life of alkaline electrolyzers. In this study, intermetallic $L1_0$-NiCo electrocatalysts were designed using DFT calculations and fabricated through a one-step solid-state reaction method. The DFT calculations indicated that $L1_0$-NiCo presented a lower H adsorption Gibbs free energy and a moderate H_2O dissociation barrier compared to the commonly used Ni catalyst and disordered NiCo alloy. Increasing the solid-state reaction temperature facilitated the formation of intermetallic $L1_0$-NiCo. Electrocatalytic tests for the alkaline HER demonstrated that the ECSA of $L1_0$-NiCo nanoparticles increased to 2.3 times, the overpotential decreased by 19%, the electrocatalytic activity increased to 1.5 times, and the stability improved to 2.2 times compared to those of the Ni nanoparticles. This research provides insights into the design and fabrication of highly efficient catalytic electrodes for alkaline electrolyzers.

1. Introduction

Utilizing renewable energy for electrocatalytic water splitting is a highly effective method for producing green hydrogen energy. Alkaline electrolyzers are the predominant technology used for this purpose, offering benefits such as low cost, high efficiency, high safety, and facile operation. Reducing energy consumption, improving hydrogen production rates, and prolonging service life are the common goals for researchers looking to enhance alkaline electrolyzers.[1–5] The alkaline HER process typically involves two electrochemical steps: the dissociation of H_2O to form adsorbed hydrogen *H and hydroxyl $*OH^-$ (the Volmer step $H_2O + e^- \rightarrow *H + *OH^-$), and the combination of *H to generate H_2 (the Heyrovsky step $H_2O + *H + e^- \rightarrow H_2 + OH^-$ or the Tafel step $*H + *H \rightarrow H_2$).[6–8] The hydrogen adsorption Gibbs free energy (ΔG_{H^*}) plays a crucial role in controlling alkaline HER activity, while the $*OH^-$ adsorption determines the rate of H_2O dissociation to provide *H.[6,7] Therefore, the design and fabrication of a suitable catalyst that facilitates the adsorption/desorption of reaction intermediates ($*OH^-$ and *H) are essential for improving the performance of alkaline electrolyzers.[3,7,8]

Nickel mesh, an economical and corrosion-resistant catalyst, has found widespread use in alkaline electrolyzers. However, pure Ni presents a strong adsorption of H and a weak capacity for H_2O dissociation, leading to an increase in energy consumption and limiting the rate of hydrogen production.[5,9] Modifying the composition and crystal structure of Ni mesh during hot forming process shows promising in enhancing electrocatalytic performance.[5,9,10] Alloying Ni with other metals like Co, Fe, Mo, Cu, Zn, and Mn can adjust the electronic structure and provide more active sites. This, in turn, improves the ability for intermediate adsorption/desorption, increases the rate and efficiency of the HER, and reduces energy consumption.[9–14] For instance, the chemically synthesized CoNi@CP electrocatalyst enhances electron transfer during the HER, regulates H adsorption, and improves catalytic performance.[15] Additionally, NiMo porous nanofibers fabricated by electrospinning and post-high-temperature oxidation reduction also exhibit strong activity in alkaline electrolytes.[16] By controlling the hot formation process to obtain ordered intermetallic like $L1_0$- and $L1_2$-phases, it is possible to effectively prevent the dissolution and precipitation of elements during the electrocatalytic process. This not only enhances electrocatalytic activity but also prolongs the service life of electrolyzers. The Pt-based intermetallic alloys with $L1_0$- or $L1_2$-phases demonstrate exceptional performance in electrocatalytic processes.[17–23] However, fewer researchers focus on the design and fabrication of intermetallic Ni alloy catalysts.

[a]*Ordos Institute of Liaoning Technical University, Ordos, 017010, China. E-mail: chun_wu@126.com*
[b]*College of Materials Science and Engineering, Liaoning Technical University, Fuxin, 123000, China*
[c]*Key Laboratory of Anisotropy and Texture of Materials (Ministry of Education), Northeastern University, Shenyang, 110819, China. E-mail: peiwl@atm.neu.edu.cn*
[d]*Science and Technology Development Corporation, Shenyang Ligong University, Shenyang, 110159, China*

† Electronic supplementary information (ESI) available. See DOI: https://doi.org/10.1039/d4nr02519a

The Co element exhibits similar hot workability to Ni, and the NiCo alloy can create both the disordered solid solution phase and the ordered intermetallic $L1_0$-phase.[24,25] In the context of the electrocatalytic alkaline HER, the presence of Co can enhance H_2O dissociation and H adsorption.[6,9] These advantages suggest that intermetallic $L1_0$-NiCo catalytic electrodes could be among the most promising candidates for enhancing the electrocatalytic performance of alkaline electrolyzers. A commonly employed strategy for designing alloy catalysts involves the use of DFT calculations, which offer a reliable explanation for the electronic structure, transition states of electrocatalytic reactions, and the impact of individual elements.[6,7] By employing DFT calculations, highly efficient NiCo alloy catalysts can be identified and designed by comparing the hydrogen adsorption Gibbs free energy (ΔG_{H^*}) and water dissociation energy of NiCo alloy models with varying structures.[6–8,26] Consequently, achieving controllable fabrication of the intermetallic $L1_0$-NiCo catalyst is crucial for reducing energy consumption, enhancing hydrogen production rates, and prolonging the service life of alkaline electrolyzers.

Wet-chemical synthesis, post-annealing, and one-step solid-state reaction methods are commonly used in the fabrication of intermetallic catalysts. However, the ordering degree of wet-chemical synthesized products often requires improvement due to limitations in synthesis temperature and diffusion rate. While post-annealing can enhance the ordering degree, it also increases the cost of fabrication.[27–30] Recently, the one-step solid-state reaction method has attracted more and more attention as it is a surfactant-free process. The higher reaction temperature in this method improves the utilization ratio of the precursor and enhances the ordering degree of the products. Some Pt-based $L1_0$-phase intermetallic nanoparticles prepared using the solid-state reaction method have demonstrated excellent magnetic and electrocatalytic properties.[21,31,32] Additionally, the parameters of the solid-state reaction process for fabricating intermetallic NiCo can serve as a guide for the hot formation process of catalytic electrodes.

In this work, the electrocatalytic alkaline HER performance of disordered solid solutions and ordered intermetallic NiCo was compared and analyzed using the DFT calculation method. The NiCo alloy nanoparticles were fabricated through the solid-state reaction method. Through comparing the electronic structure, microstructure, and electrocatalytic HER performance, a Ni alloy catalyst suitable for alkaline HER electrocatalysis was designed and fabricated. This study aims to enhance hydrogen production rates, reduce energy consumption, and prolong the service life of alkaline electrolyzers.

2. Research methods

2.1 Design of a NiCo alloy

All static calculations in this paper were carried out using density functional theory (DFT) and VASP 5.4.4 (Vienna *ab initio* simulation software package). The generalized gradient approximation (GGA) PBE (Perdew Burke Ernzerhof exchange–correlation) was employed for computing the exchange–correlation energy. The plane wave basis cutoff energy was set at 500 eV. The Brillouin zone integration was optimized using a $5 \times 5 \times 5$ k grid for the initial model and a $4 \times 4 \times 1$ k grid for the section model. The atomic positions and horizontal lattice parameters were optimized using the conjugate gradient algorithm. The convergence criteria for energy and force were set to 1.0×10^{-6} eV and -0.01 eV Å^{-1}, respectively. The calculation focused on the (111) plane of a NiCo alloy with both face-centered cubic (fcc) and face-centered tetragonal (fct) structures.

2.2 Synthesis of the NiCo alloy

The NiCo alloy catalyst was fabricated using a medium-assisted solid-state reaction method. Firstly, an equimolar amount of nickel acetylacetonate ($Ni(acac)_2$) and cobalt acetylacetonate ($Co(acac)_3$) precursors were dissolved in n-hexane and ethanol, and stirred at 50 °C to create a homogeneous precursor solution. Solid NaCl powder, ground to a particle size of less than 9 ± 1 μm, was used as an isolation medium. Approximately 300 times the mass of the precursors in NaCl powder was added to the precursor solution, which was then slowly dried at 80 °C. The obtained NaCl–precursor mixed powder was transferred to a tube furnace under a reducing atmosphere (90% Ar + 10% H_2). The mixed powder was heated to either 500 °C or 780 °C at a rate of 10 °C min^{-1} and held for 180 minutes. Subsequently, the black mixed powder was dissolved in deionized water, and the NiCo alloy was obtained through multiple centrifugations with ethanol, and then stored in ethanol at −20 °C.

2.3 Microstructure and property detection of the NiCo alloy

The crystal structure of the NiCo alloy was analyzed using a Rigaku D/Max 2400 diffractometer with Cu Kα X-ray diffraction (XRD) in the 2θ range of 30°–80°. The morphology and size of nanoparticles were observed using a JEM-2100F field emission transmission electron microscope (TEM) produced by JEOL in Japan. High-resolution transmission electron microscopy (HRTEM) was used to analyze crystal plane spacing. To clarify the coordination state of elements in the NiCo alloy, X-ray absorption near edge spectroscopy (XANES) was performed at the Ni K edge using a commercial synchrotron radiation experimental device (Easy XAFS300, XAFS LLC, Renton). During the analysis, the S_0^2 was set to 1.0, and the data ranges considered were $3.0 < k \leq 12.0$ Å^{-1} and $1.0 < R < 3$ Å in the fitting process.

The electrochemical performance was tested using a three-electrode system on a CS2350H electrochemical workstation in a 1 M KOH electrolyte. The counter electrode was a carbon rod, the reference electrode was a mercury oxide electrode, and the working electrode was a glassy carbon electrode with a 3 mm diameter loaded with the alloy catalyst. Approximately 2 mg of the alloy catalyst was dispersed in 196 μL of isopropanol and 4 μL of Nafion solution, and then sonicated for 45 minutes until the alloy particles were uniformly dispersed.

Subsequently, 7 μL of the solution was dropped on the glassy carbon electrode, resulting in a catalyst loading of about 1 mg cm^{-2}. The polarization curve (LSV) was measured at a scan rate of 5 mV s^{-1} in 1 M KOH alkaline medium. The electric double-layer capacitance (C_{dl}) of the nanoparticles was measured by cyclic voltammetry from 0.38 V to 0.48 V at a scan rate ranging from 25 to 125 mV s^{-1}. The electrochemical surface area (ECSA) was calculated as ECSA = C_{dl}/C_s, where C_s = 0.04 mF cm^{-2} representing the general specific capacitance. The electrochemical impedance spectroscopy (EIS) testing was performed at a current density of 10 mA cm^{-2} and a frequency range of 0.1–100 kHz. The long-term stability of the NiCo alloy was evaluated by monitoring the overpotential for about 10 hours at current densities of 10 and 100 mA cm^{-2}.

3. Results and discussion

3.1 Electronic structure analysis and discussion

The 2 × 2 × 2 supercell models of Ni, disordered NiCo solid solution, and ordered intermetallic $L1_0$-NiCo are shown in Fig. 1(a)–(c). In the disordered NiCo solid solution, Ni and Co atoms are randomly distributed, whereas in the $L1_0$-phase they are arranged periodically along the ⟨001⟩ direction. Following geometric optimization, the lattice parameters of the disordered NiCo solid solution are $a = c$ = 3.43 Å, while for $L1_0$-NiCo they are a = 3.39 Å and c = 3.49 Å. The a-axis is compressed and the c-axis is expanded after the disorder–order transition.[33,34] The adsorption of H_2O on the catalyst surface initiates the electrocatalytic alkaline HER, with the dissociation of H_2O to $*OH^-$ and *H being a rate-determining step.[6,7] Fig. 1(d) shows the energy distribution of the H_2O dissociation process on Ni, disordered NiCo solid solution, and ordered intermetallic $L1_0$-NiCo. The transition state barrier ΔE for H_2O dissociation on the $L1_0$-NiCo surface is 0.508 eV, lower than those of Ni (0.706 eV) and NiCo solid solution (0.655 eV). The incorporation of Co into Ni and the formation of the $L1_0$-phase both enhance the H_2O dissociation process. The most favorable transition state barrier is observed on the $L1_0$-NiCo surface. The lowest transition state barrier is observed on the $L1_0$-NiCo surface. After the H_2O dissociation, the energy of *H and $*OH^-$ on the $L1_0$-phase surface is about −0.464 eV, closer to 0 compared to those of Ni (−0.637 eV) and NiCo solid solution (−0.528 eV), indicating that H_2O dissociation is more favorable on the intermetallic $L1_0$-NiCo surface. Another important step in the electrocatalytic alkaline HER process is the reduction of *H. This reduction can be evaluated from the Gibbs free energy of hydrogen adsorption $\Delta G_{H^*} = E_H + \Delta E_{ZPE} - T\Delta S_H$, where ΔE_H represents the binding energy of hydrogen, ΔE_{ZPE} is the zero-point energy difference between adsorbed hydrogen and gaseous hydrogen, and $T\Delta S_H$ is the entropy difference between these two states. The closer ΔG_{H^*} is to 0, the more efficient the HER activity.[7,35–37] In Fig. 1(e), it is observed that the ΔG_{H^*} value for $L1_0$-NiCo is closer to 0 (−0.537 eV) compared to those of Ni (−0.708 eV) and NiCo solid solution (−0.628 eV). This suggests that the *H reduction is also more favorable on the $L1_0$-NiCo surface. In conclusion, the HER performance of Ni can be improved by alloying with the Co element and the formation of the $L1_0$-phase. The intermetallic $L1_0$-NiCo catalyst exhibits superior catalytic performance.[11,33]

The projected density of states (PDOS) distributions of Ni, disordered NiCo solid solution, and ordered intermetallic $L1_0$-NiCo are shown in Fig. 2. The 3d orbitals of Ni and Co

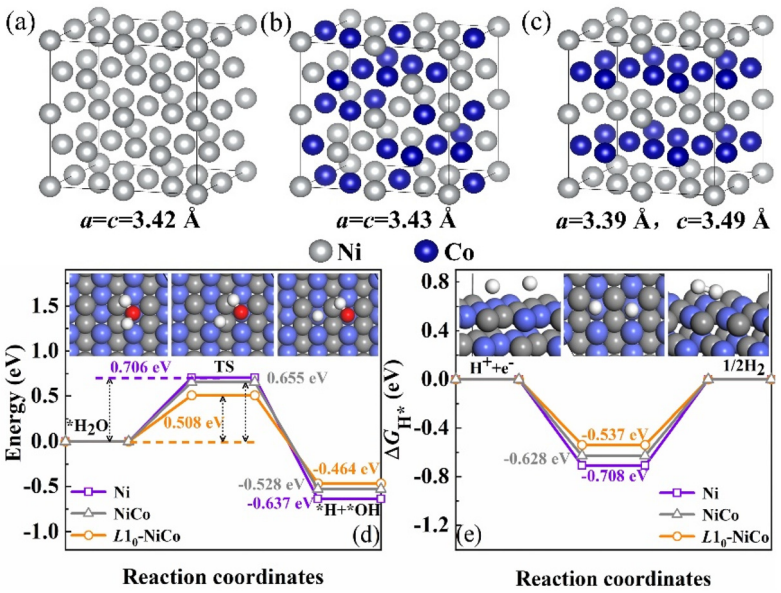

Fig. 1 (a) Ni, (b) disordered NiCo solid solution, and (c) and ordered intermetallic $L1_0$-NiCo 2 × 2 × 2 supercell. (d) The energy difference of the H_2O dissociation process. (e) H adsorption Gibbs free energy diagram.

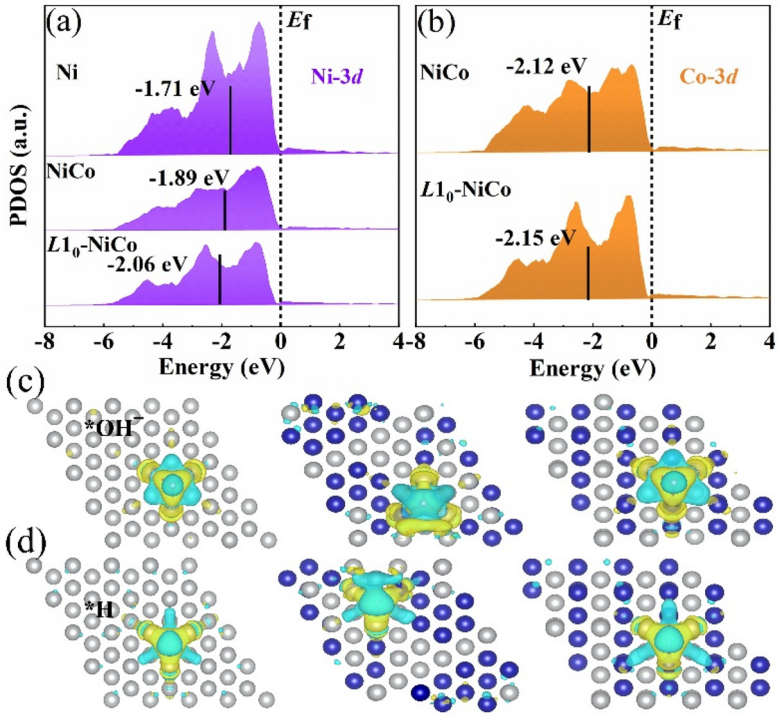

Fig. 2 (a) The density of states and d-band center of Ni and (b) Co atoms, (c) the differential charge density diagram of *OH$^-$ and (d) *H of Ni, disordered NiCo solid solution and ordered intermetallic $L1_0$-NiCo.

elements play a dominant role in the alkaline HER electrocatalytic process. As shown in Fig. 2(a), the 3d orbital of Ni crosses the Fermi level and shows a sharp peak.[6,26] Upon alloying Ni with Co atoms, the peak intensities of the Ni-3d orbital weakens and shifts towards the left-side, resulting in a more uniform electron energy distribution. This indicates a reduction in the strong adsorption of Ni and an optimization of the adsorption ability.[38,39] The $L1_0$-NiCo structure, with its sharper Co-3d orbital, shows a more stable electronic configuration compared to the disordered NiCo solid solution. Furthermore, the d-band center of Ni-3d shifts downwards from −1.89 to −2.06 eV, and the d-band center of Co-3d shifts from −2.12 to −2.15 eV, moving further away from the Fermi level. This shift suggests a higher distribution of electrons on the bonding orbitals in $L1_0$-NiCo, enhancing electron storage and ultimately leading to increased electrocatalytic activity.[6,40,41]

The H_2O dissociation and *H combination are two crucial rate-determining steps in the electrocatalytic alkaline HER process. On the catalyst surface, *OH$^-$ and *H are produced following H_2O dissociation. Fig. 2(c) shows the charge density of *OH$^-$ generated on Ni, disordered NiCo solid solution, and $L1_0$-NiCo surfaces. The *OH$^-$ is adsorbed at the fcc-site, with the O atom bonding to adjacent metal atoms and the H atom located on the O atom to create a stable structure. Upon alloying Ni with Co, the notably expanded yellow region in the differential charge indicates an increased adsorption strength of *OH$^-$ and stronger atom interactions. In comparison with disordered NiCo, *OH$^-$ adsorption on $L1_0$-NiCo is more uniform and orderly. This uniform adsorption state suggests a decrease in energy release on $L1_0$-NiCo, facilitating H_2O dissociation and *H formation. Consequently, the H_2O dissociation barrier on the surface of $L1_0$-NiCo is the lowest. The *H generated from H_2O dissociation will combine and desorb to produce H. During desorption, *H can be adsorbed by multiple adjacent atoms, and the binding energy of *H is influenced by the interaction with these atoms.[6,7] Fig. 2(c) shows the differential charge density of *H on the Ni, disordered NiCo solid solution, and $L1_0$-NiCo surfaces. The *H is also adsorbed at the fcc site and forms a stable structure by binding with three adjacent metal atoms. The adsorption of *H is found to be more stable than that of *OH$^-$, indicating a stronger charge transfer and interaction between *H and the catalyst.[6,42] When comparing the disordered NiCo solid solution with $L1_0$-NiCo, it is observed that *H adsorption on $L1_0$-NiCo is more susceptible to the influence of surrounding atoms and tends to reach a relatively complete adsorption state. This suggests that $L1_0$-NiCo generates more surface-active sites, facilitating the adsorption and charge transfer of *H.[42] Consequently, alloying Ni with Co and forming the intermetallic $L1_0$-NiCo results in an increase in ΔG_{H^*} to nearly 0, thereby enhancing the HER catalytic performance.

Fig. 3(a) shows the XRD patterns of Ni and NiCo alloys. Three diffraction peaks of Ni are observed at about 45.51°, 51.83°, and 76.43° when the solid-reaction temperature is 500 °C, corresponding to the (111), (200), and (220) planes of

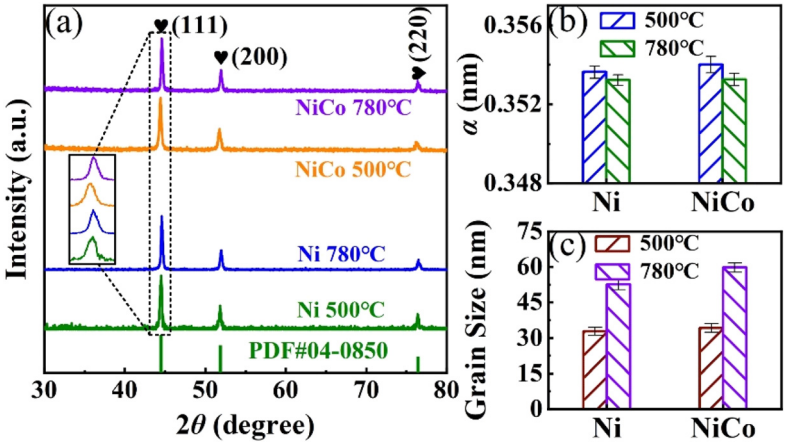

Fig. 3 (a) XRD patterns, (b) lattice parameters, and (c) grain sizes of Ni and NiCo alloys fabricated at different temperatures.

the fcc structure. After alloying with Co, the (111) peak of Ni shifts to the left by 0.03°. Upon increasing the solid-reaction temperature to 780 °C, the (111) peak of Ni shifts to the right by 0.07°, while the (111) peak of the NiCo alloy shifts to the right by 0.06°. The lattice parameter a of Ni and NiCo alloys is calculated from the (111) and (200) peaks, as shown in Fig. 3(b). The a of the NiCo alloy is larger than that of Ni, due to the larger atomic radius of Co compared to that of Ni, resulting in the expansion of the Ni lattice upon alloying with Co. With an increase in a and interplanar spacing, the diffraction peaks shift towards a lower diffraction angle. Conversely, raising the reaction temperature from 500 °C to 780 °C causes the diffraction peaks of Ni and NiCo alloys to shift towards higher diffraction angles, indicating lattice compression. Nanoparticles nucleate and grow on the surface of the isolation medium (NaCl) in the solid-state reaction process. Since the thermal expansion coefficient of the NiCo alloy is larger than that of NaCl, the growth process is compressed by the NaCl matrix. The difference in thermal expansion coefficients between the nanoparticles and matrix is amplified with a temperature increase, leading to heightened compressive stress and a decrease in a.[15,16] The grain sizes D of Ni and NiCo alloy nanoparticles were calculated using the Scherrer formula, where $D = K\lambda/(\beta \cos\theta)$, with $K = 0.89$ as a constant, $\lambda = 0.154$ nm as the X-ray wavelength, β as the full width at half maximum, and θ as the diffraction angle. The grain size of NiCo nanoparticles, as illustrated in Fig. 3(c), is similar to that of Ni following the addition of Co due to an equal total amount of precursors in the solid-state reaction. The grain sizes of Ni and NiCo alloy nanoparticles increase with the increase of solid-state reaction temperature, because the ripening growth rates increases with temperature.[21,29] It is important to note that the XRD patterns do not exhibit the characteristic peaks of the $L1_0$-phase, a result consistent with other studies due to the similar electron numbers and X-ray scattering factors of Ni and Co.[16,37] Nevertheless, the right-shift of diffraction peaks and increased stress with rising solid-state reaction temperature suggest the possibility of disorder–order transition in the NiCo nanoparticles.

To further analyze the ordered $L1_0$-phase characteristics of NiCo alloys fabricated by solid-state reaction at high temperature, the coordination state of Ni atoms in disordered NiCo solid solution and intermetallic $L1_0$-NiCo was analyzed using DFT calculations, as shown in Fig. 4(a). In the disordered NiCo solid solution, the bond lengths of Ni–Ni and Ni–Co are approximately 2.42 Å, whereas in the intermetallic $L1_0$-NiCo, these bond lengths are 2.37 Å and 2.41 Å, respectively. The shorter bond lengths in $L1_0$-NiCo indicate a closer arrangement of atoms.[42–46] The formation energy of disordered NiCo solid solution and $L1_0$-NiCo was calculated using $\Delta E_{form} = \Delta E_{total} - n\mu_x$, where ΔE_{total} represents the system energy of the NiCo alloy, μ_x is the chemical potential of the x atom, and n is the number of x atoms. As shown in Fig. 4(b), the ΔE_{form} decreases after the formation of the ordered intermetallic, indicating that $L1_0$-NiCo presents enhanced thermal stability.[44] The formation of $L1_0$-NiCo is favored at higher temperatures that can overcome the energy barrier. The local structure information of Ni in the NiCo alloy was analyzed using synchrotron radiation X-ray absorption spectroscopy. The Ni K edge X-ray absorption near-edge structure (XANES) spectra of Ni foil and the NiCo alloy fabricated at various temperatures are presented in Fig. 4(c). Both the NiCo alloy and Ni foil exhibit a similar edge-front peak feature at 8335 eV and a white line peak at 8350 eV, arising from the 1s → 3d and 1s → 4p$_z$ electronic transition, respectively. This indicates that the atoms are in a metallic state and Ni–Co bonds are formed in the NiCo alloy.[43] A comparison with the Ni foil reveals increased white line peak intensities and a decreased Ni valence state in the NiCo alloy, suggesting electron transfer between Ni and Co. Moreover, while the white line peak of the Ni foil displays a noticeable splitting, the NiCo alloys show less splitting, attributed to the fcc structure of Ni and the influence of Co alloying on the electron configuration of Ni. In Fig. 4(d), the oscillation curves of Ni K edge XAFS $K^3\chi$ in the Ni foil and NiCo alloys are

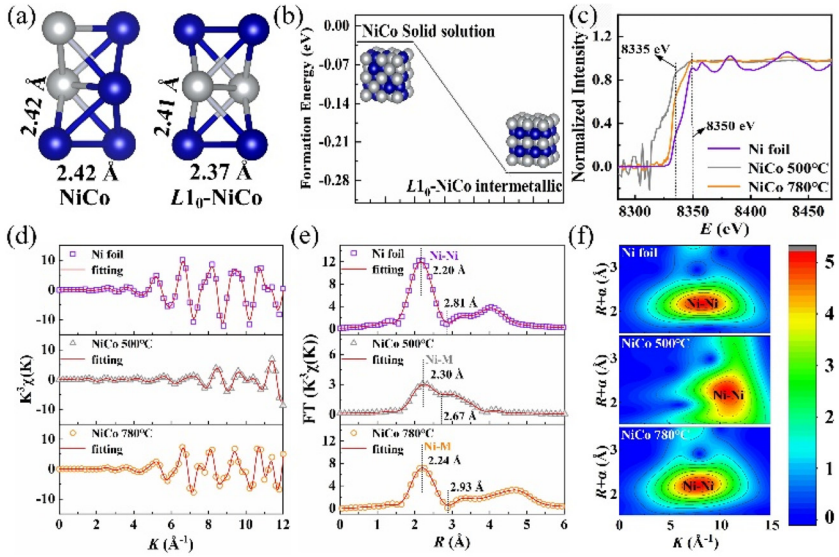

Fig. 4 (a) Ni–Ni and Ni–Co bond length of the Ni foil and NiCo alloy. (b) The formation energy of disordered NiCo solid solution and intermetallic $L1_0$-NiCo. (c) Ni K-edge XANES spectrum, (d) oscillation curve of the Ni K edge XAFS $K^3\chi$ (K), (e) Fourier transform of Ni K-edge EXAFS spectra and (f) EXAFS wavelet transform diagram of the Ni foil and NiCo alloy.

depicted. The oscillation peak intensity of the NiCo alloy at 500 °C is notably lower than that at 780 °C, indicating that increasing the temperature enhances atomic interactions and reduces the bond length of Ni–Co. The stronger Ni–Co coordination observed at 780 °C suggests improved crystal structure stability, consistent with the characteristics of the intermetallic $L1_0$-phase.

The extended X-ray absorption fine structure (EXAFS) was employed to examine bond lengths and coordination numbers (CN). Fig. 4(e) and Table 1 illustrate that the Ni–M bond length in the NiCo alloy is longer and the diffraction peak intensities are weaker compared to those in the Ni foil (2.20 Å), attributed to the larger atomic radius of the alloying element Co.[42,43] Increasing the solid-state reaction temperature from 500 °C to 780 °C results in higher peak intensities of the Ni–M bond, a decrease in the bond length of Ni–M in the NiCo alloy from 2.30 to 2.24 Å, and a decrease in CN from 11.5 to 7.9 (close to 8 in the $L1_0$-phase). These findings align with DFT calculation results and suggest the formation of intermetallic $L1_0$-CoNi nanoparticles at 780 °C. The wavelet transform spectrum (Fig. 4(f)) indicates that the maximum strength of the Ni–M bond in the NiCo alloy is about 2.20 Å, similar to that of the Ni foil. Moreover, the Ni–M bond length in the NiCo alloy at 500 °C shows instability, consistent with formation energy calculations. The thermal stability at high temperatures leads to the stable formation of the $L1_0$ ordered structure. While the characteristic diffraction peaks of $L1_0$-NiCo are not observable due to X-ray limitations, the edge-front peak characteristics of synchrotron radiation, along with the lengths, intensities, and CN of Ni–M bonds, suggest the formation of intermetallic $L1_0$-NiCo upon increasing the solid-state reaction temperature to 780 °C.

Table 1 Structure parameters and fitting parameters of Ni K-edge EXAFS data

Samples	Bond	*CN*	Bond length/Å	σ^2/(Å^2)	Δ*E*/eV	*R*-factor
Ni-foil	Ni–Ni	12	2.81	0.0059	7.815	0.007
NiCo-500 °C	Ni–M	11.5	2.67	0.047	5.863	0.01
NiCo-780 °C	Ni–M	7.9	2.93	0.0051	7.78	0.008

The TEM images of Ni and NiCo alloys synthesized at various solid-state reaction temperatures are shown in Fig. 5 (a_1)–(d_1). The Ni and NiCo nanoparticles show a spherical morphology without obvious sintering. The sizes of the alloy nanoparticles, ranging from 30 to 60 nm, align with the grain size calculated using the Scherrer formula (Fig. 3(c)), indicating their monocrystalline nature. High-resolution TEM images in Fig. 5(a_2)–(d_2) reveal parallel lattice fringes across the particles, further confirming their monocrystalline structure. Fourier transform analysis in Fig. 5(a_3)–(d_3) shows interplanar distances as the spacing between dark and bright stripes. Alloying Ni with the Co element and reducing the solid-state reaction temperature result in an increased interplanar distance and lattice constant, consistent with the XRD results.

Fig. 6(a) shows the electrochemical double layer current (*i vs.* scan rate) obtained by collecting the CV data of Ni and NiCo alloy nanoparticles at a scan rate of 25–125 mV s^{-1}. Alloying Ni with Co and increasing the solid-state reaction temperature resulted in an increase in the C_{dl}, with $L1_0$-NiCo exhibiting the highest C_{dl} value of 4.90 mF. The ECSA of Ni and NiCo alloys was calculated using the formula ECSA = C_{dl}/C_s and is shown in Fig. 6(c). The NiCo alloys show a higher

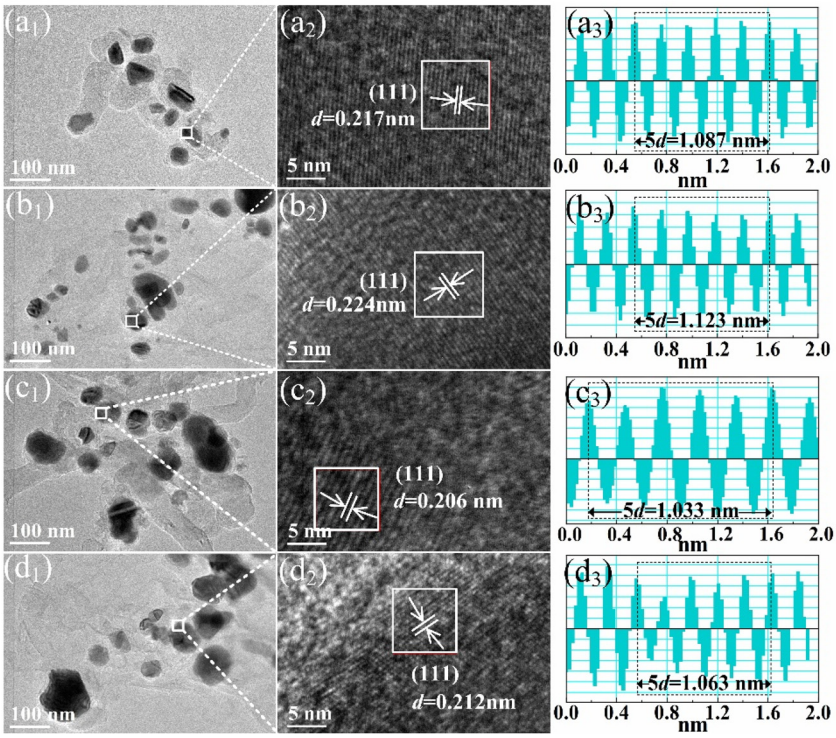

Fig. 5 TEM image (1), HRTEM image (2) and the Fourier transform diagram (3) of Ni and NiCo alloys fabricated at different temperatures. (a) Ni-500 °C, (b) NiCo-500 °C, (c) Ni-780 °C, and (d) NiCo-780 °C.

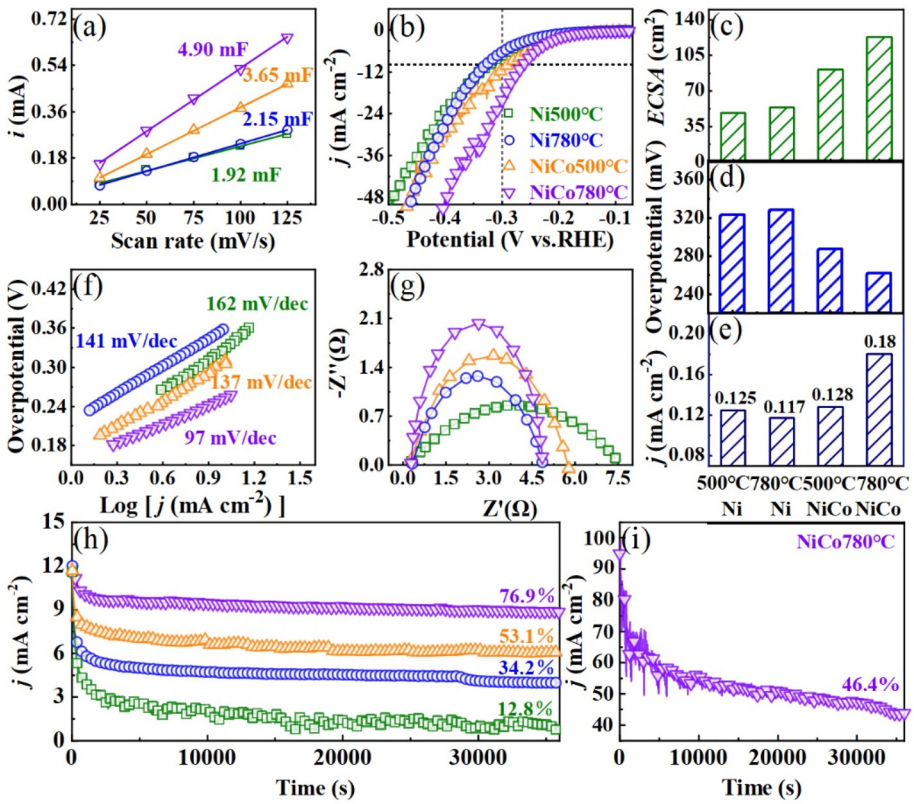

Fig. 6 (a) Electric double layer capacitance, (b) LSV curve, (c) ECSA, (d) overpotential at 10 mA cm^{-2}, (e) area activity at −0.3 V, (f) Tafel slope, and (g) electrochemical impedance of Ni and NiCo alloy catalysts. (h) Stability test of Ni and NiCo alloy catalysts at 10 mA cm^{-2} and (i) stability test of $L1_0$-NiCo alloys at 100 mA cm^{-2}.

ECSA compared to Ni, and it increases with the increase of temperature. $L1_0$-NiCo reaches a maximum ECSA of 122.5 cm^2, approximately 2.3 times that of Ni nanoparticles. The 3d-orbital electron distributions and d-band center evolution in DFT calculations also suggest that the active sites on the surface of $L1_0$-NiCo are the most abundant.[39,40] Fig. 6(b) shows the ECSA normalized HER polarization curves of Ni and NiCo alloys. At a current density of 10 mA cm^{-2}, the overpotentials of Ni and NiCo nanoparticle catalysts fabricated at 500 °C are 361 and 300 mV, respectively. As shown in Fig. 6(d), increasing the temperature to 780 °C reduces the overpotentials to 323 and 262 mV, with intermetallic $L1_0$-NiCo nanoparticles exhibiting the lowest overpotential, about 81% that of the Ni catalyst. It means that the energy consumption of alkaline electrolyzers will be reduced when using $L1_0$-NiCo as the HER catalyst.[12,15,16] The area activities of Ni and NiCo alloys at −0.3 V are shown in Fig. 6(e). The Ni and NiCo nanoparticles fabricated at 500 °C displayed area activities of 0.125 and 0.128 mA cm^{-2}, respectively. At 780 °C, these values changed to 0.117 and 0.180 mA cm^{-2}. $L1_0$-NiCo demonstrated the highest area activity, approximately 1.5 times that of the Ni catalyst, suggesting an enhancement in the hydrogen production rate of alkaline electrolyzers when employing $L1_0$-NiCo as an HER catalyst.

The Tafel slope was calculated from the LSV curve to illustrate the HER kinetics of Ni and the NiCo alloy. In Fig. 6(f), it is observed that the Tafel slopes of Ni and NiCo nanoparticle catalysts fabricated at 500 °C are 162 and 137 mV dec^{-1} respectively, and decrease to 141 and 97 mV dec^{-1} when the temperature is raised to 780 °C. The HER kinetics of Ni nanoparticles follow the Heyrovsky process (>120 mV dec^{-1}), similar to that of nickel foam catalysts.[12,15,16] With the increase of solid-state reaction temperature, the HER kinetics of $L1_0$-NiCo transitions from the Heyrovsky to the Volmer–Heyrovsky process, where the rate-determining step of the Volmer reaction consistently displays a faster HER reaction rate.[6] The formation of the ordered $L1_0$-phase enhances the reaction rate by optimizing the HER kinetics. Electrochemical impedance spectroscopy (EIS) analysis was performed on Ni and NiCo alloys to further understand the interface reaction in the HER process, as shown in Fig. 6(g). Alloying Ni with Co and increasing the temperature can reduce the radius of the semicircle in the Nyquist diagram. This reduction in radius signifies a decrease in surface charge transfer resistance, and facilitates charge transfer during the HER process.[42,43,47] This result is consistent with the evaluation of state densities in DFT calculations, indicating that the enhancement of electron storage in $L1_0$-NiCo leads to a reduction in charge transfer resistance and overpotential. The chronoamperometry curve of Ni and NiCo alloys in 1 M KOH at a current density of 10 mA cm^{-2} is shown in Fig. 6(h). After 10 hours of discharge, the Ni and NiCo nanoparticles fabricated at 500 °C maintain only 12.8% and 53.1% activities, respectively, which increase to 34.2% and 76.9% when fabricated at 780 °C. At a higher current density of 100 mA cm^{-2}, as shown in Fig. 6(i), the $L1_0$-NiCo alloy still retains 46.4% activity after 10 hours of discharge, while the disordered NiCo solid solution cannot work at this higher current. Alloying Ni with Co and increasing the solid phase reaction temperature enhance the stability of the catalyst. $L1_0$-NiCo demonstrates the best stability, about 2.2 times that of Ni, due to its greater thermodynamic stability. This suggests that employing $L1_0$-NiCo as an HER catalyst could prolong the service life of alkaline electrolyzers.

4. Conclusion

In this paper, the DFT calculation method was employed to analyze the electrocatalytic performance of Ni, disordered NiCo solid solution, and ordered intermetallic $L1_0$-NiCo catalysts for the alkaline HER. Adding Co into the Ni catalyst and forming intermetallic $L1_0$-NiCo resulted in a reduction of the d-band center, enhanced electron storage, lowered H_2O dissociation barrier, increased H adsorption Gibbs free energy closer to 0, and decreased formation energy, ultimately improving the electrocatalytic activity and stability. The designed $L1_0$-NiCo catalyst was successfully fabricated through a solid-state reaction method. Raised reaction temperatures increased compressive stress, leading to a decrease in the lattice constant and facilitating $L1_0$-phase formation. Compared to Ni nanoparticles, fabricated and tested under the same conditions, the ECSA of $L1_0$-NiCo nanoparticles increased to about 2.3 times, overpotential reduced by 19%, electrocatalytic activity improved to 1.5 times, and stability was increased to 2.2 times under similar conditions. The DFT calculation and experimental results suggested that employing $L1_0$-NiCo as a catalytic electrode in alkaline electrolyzers could yield benefits such as reduced energy consumption, enhanced hydrogen production rates, and prolonged service life. The intermetallic $L1_0$-NiCo would be a reliable and efficient option for alkaline electrolyzers.

Author contributions

Chun Wu: writing – original draft, writing – review & editing, project administration, supervision, and funding acquisition. Xuhui Wang: writing – original draft, data curation, software, and formal analysis. Mengyao Huang, Chao Meng and Ling Chang: investigation, data curation, and formal analysis. Dake Xu and Wenli Pei: writing – review & editing, project administration, supervision, and funding acquisition.

Data availability

The data supporting this article have been included as part of the ESI.†

Conflicts of interest

There are no conflicts to declare.

Acknowledgements

This work was financially supported by the National Key Research and Development Program of China (No. 2020YFA0907300 and 2021YFB3501404), the National Natural Science Foundation of China (Grant No. 52071070, 52102360 and 52371179), the China Postdoctoral Science Foundation (Grant No. 2023M732392), the Opening Fund of Key Laboratory of Electromagnetic Processing of Materials (Grant No. NEU-EPM-025), and the Key Scientific Research Projects of Ordos Institute-LNTU (Grant No. YJY-ZD-2023-001).

References

1 P. Liu, J. Wang, X. Wang, L. Liu, *et al.*, A superhydrophilic NiFe electrode for industrial alkaline water electrolysis, *Int. J. Hydrogen Energy*, 2023, **7**, 253, DOI: **10.1016/j.ijhydene.2023.07.253**.

2 Z. Zhu, Y. Lin, P. Fang, M. Wang, *et al.*, Orderly nanodendritic nickel substitute for raney nickel catalyst improving alkali water electrolyser, *Adv. Mater.*, 2023, 2307035, DOI: **10.1002/adma.202307035**.

3 C. Hu, C. Lv, N. Zeng, A. Liu, *et al.*, Recent advances in Ni–based electrocatalysts for hydrogen evolution reaction, *Energy Technol.*, 2023, **11**, 2201048, DOI: **10.1002/ente.202201048**.

4 J. Liu, Z. Wang, D. Zhang, Y. Qin, *et al.*, Systematic engineering on Ni–based nanocatalysts effectively promote hydrogen evolution reaction, *Small*, 2022, **18**, 2108072, DOI: **10.1002/smll.202108072**.

5 J. Shen, Q. Jin, C. Chen, S. Xu, *et al.*, A strategy for improving the stability of platinum-containing electrocatalyst toward hydrogen production in industrial alkaline water electrolysis, *Appl. Phys. Lett.*, 2023, **123**, 133902, DOI: **10.1063/5.0169722**.

6 J. Wang, S. Xin, Y. Xiao, Z. Zhang, *et al.*, Manipulating the water dissociation electrocatalytic sites of bimetallic Nickel-Based alloys for highly efficient alkaline hydrogen evolution, *Angew. Chem., Int. Ed.*, 2022, **61**, e202202518, DOI: **10.1002/anie.202202518**.

7 C. Wei, Y. Sun, G. n. G. Scherer, A. C. Fisher, *et al.*, Surface composition dependent ligand effect in tuning the activity of nickel–copper bimetallic electrocatalysts toward hydrogen evolution in alkaline, *J. Am. Chem. Soc.*, 2020, **142**, 7765–7775, DOI: **10.1021/jacs.9b12005**.

8 X. Zhang, J. Wang, J. Wang, J. Wang, *et al.*, Freestanding surface disordered NiCu solid solution as ultrastable high current density hydrogen evolution reaction electrode, *J. Phys. Chem. Lett.*, 2021, **12**, 11135–11142, DOI: **10.1021/acs.jpclett.1c03041**.

9 Y.-C. Zhang, C. Han, J. Gao, L. Pan, *et al.*, NiCo-based electrocatalysts for the alkaline oxygen evolution reaction: a review, *ACS Catal.*, 2021, **11**, 12485–12509, DOI: **10.1021/acscatal.1c03260**.

10 D. Li, B. Zhang, Y. Li, R. Chen, *et al.*, Boosting hydrogen evolution activity in alkaline media with dispersed ruthenium clusters in NiCo-layered double hydroxide, *Electrochem. Commun.*, 2019, **101**, 23–27, DOI: **10.1016/j.elecom.2019.01.014**.

11 T. Sun, J. Cao, J. Dong, H. Du, *et al.*, Ordered mesoporous NiCo alloys for highly efficient electrocatalytic hydrogen evolution reaction, *Int. J. Hydrogen Energy*, 2017, **42**, 6637–6645, DOI: **10.1016/j.ijhydene.2017.01.071**.

12 J. Dong, T. Sun, Y. Zhang, H. Zhang, *et al.*, Mesoporous NiCo alloy/reduced graphene oxide nanocomposites as efficient hydrogen evolution catalysts, *J. Colloid Interface Sci.*, 2021, **599**, 603–610, DOI: **10.1016/j.jcis.2021.04.124**.

13 C. Zhou, J. Y. Zhao, P. F. Liu, J. Chen, *et al.*, Towards the object-oriented design of active hydrogen evolution catalysts on single-atom alloys, *Chem. Sci.*, 2021, **12**, 10634–10642, DOI: **10.1039/D1SC01018B**.

14 Y. Zhou, T. Lin, X. Luo, Z. Yan, *et al.*, Mechanistic study on nickel-molybdenum based electrocatalysts for the hydrogen evolution reaction, *J. Catal.*, 2020, **388**, 122–129, DOI: **10.1016/j.jcat.2020.05.011**.

15 C. Yu, X. Zhai, P. Wu, Z. Zhu, *et al.*, CoNi alloy nanoparticles coated with carbon layer doped with P atom for efficient hydrogen evolution reaction, *Int. J. Hydrogen Energy*, 2021, **46**, 36753–36762, DOI: **10.1016/j.ijhydene.2021.08.217**.

16 M. Sun, Q. Ye, L. Lin, Y. Wang, *et al.*, NiMo solid-solution alloy porous nanofiber as outstanding hydrogen evolution electrocatalyst, *J. Colloid Interface Sci.*, 2023, **637**, 262–270, DOI: **10.1016/j.jcis.2023.01.094**.

17 Z. Meng, F. Xiao, Z. Wei, X. Guo, *et al.*, Direct synthesis of $L1_0$-FePt nanoparticles from single-source bimetallic complex and their electrocatalytic applications in oxygen reduction and hydrogen evolution reactions, *Nano Res.*, 2019, **12**, 2954–2959, DOI: **10.1007/s12274-019-2537-y**.

18 A. Belozerov, A. Katanin and V. Anisimov, Coulomb correlations and magnetic properties of $L1_0$-FeCo: A DFT+DMFT study, *Phys. Rev. Mater.*, 2022, **6**, 055004, DOI: **10.48550/arXiv.2202.03205**.

19 D. Zhou, G. Zhang, Y. Li, S. Liu, *et al.*, Enriching Pt3 ensemble with isolated 3-fold hollow site by crystal-phase engineering of Pt3Fe single-nanoparticle for acetylene hydrogenation, *Chem. Eng. J.*, 2023, **472**, 144875, DOI: **10.1016/j.cej.2023.144875**.

20 J. Zhou, X. Chen, M. Guo, W. Hu, *et al.*, Enhanced Catalytic Activity of Bimetallic Ordered Catalysts for Nitrogen Reduction Reaction by Perturbation of Scaling Relations, *ACS Catal.*, 2023, **13**, 2190–2201, DOI: **10.1021/acscatal.2c05877**.

21 S. Dong, Y. Ju, Y. Jiang, C. Meng, *et al.*, Effects of solid isolation medium on the microstructure and magnetic properties of one-step sintered $L1_0$-FePtCu nanoparticles, *J. Alloys Compd.*, 2022, **909**, 164748, DOI: **10.1016/j.jallcom.2022.164748**.

22 W. Pei, D. Zhao, C. Wu, Z. Sun, *et al.*, Direct synthesis of $L1_0$-FePt nanoparticles with high coercivity via Pb addition

for applications in permanent magnets and catalysts, *ACS Appl. Nano Mater.*, 2020, **3**, 1098–1103, DOI: **10.1021/acsanm.9b02420**.

23 C. Wu, Y. Jiang, Z. Niu, D. Zhao, *et al.*, Effects of high magnetic field annealing on FePt nanoparticles with shape-anisotropy and element-distribution-anisotropy, *RSC Adv.*, 2021, **11**, 10463–10467, DOI: **10.1039/d1ra00072a**.

24 T. Omori, K. Oikawa, J. Sato, *et al.*, Partition behavior of alloying elements and phase transformation temperatures in Co-Al-W-base quaternary systems, *Intermetallics*, 2013, **3**, 274–283, DOI: **10.1016/j.intermet.2012.07.033**.

25 P. Liu, L. Li, S. Yu, *et al.*, Effect of transition metal element additions on the mechanical and electronic properties of $L1_0$ CoNi alloys, *Extreme Mech. Lett.*, 2021, **42**, 101128, DOI: **10.1016/j.eml.2020.101128**.

26 J. Mou, Y. Gao, J. Wang, J. Ma, *et al.*, Hydrogen evolution reaction activity related to the facet-dependent electrocatalytic performance of NiCoP from first principles, *RSC Adv.*, 2019, **9**, 11755–11761, DOI: **10.1039/c9ra01560d**.

27 W. Pei, D. Zhao, C. Wu, X. Wang, *et al.*, Facile liquid-assisted one-step sintering synthesis of superfine $L1_0$-FePt nanoparticles, *RSC Adv.*, 2019, **9**, 36034–36039, DOI: **10.1039/c9ra06966f**.

28 D. Zhao, X. Wang, L. Chang, W. Pei, *et al.*, Synthesis of super-fine $L1_0$-FePt nanoparticles with high ordering degree by two-step sintering under high magnetic field, *J. Mater. Sci. Technol.*, 2021, **73**, 178–185, DOI: **10.1016/j.jmst.2020.09.026**.

29 C. Wu, D. Zheng, X. Wang, D. Zhao, *et al.*, Effects of high magnetic field on the growth and magnetic property of $L1_0$-FePtCu nanoparticles, *J. Magn. Magn. Mater.*, 2021, **526**, 167731, DOI: **10.1016/j.jmmm.2021.167731**.

30 K. Yamagiwa and J. Kuwanos, One-step liquid-phase synthesis of platinum nanocatalysts supported on aligned carbon nanotube arrays, *Mater. Chem. Phys.*, 2018, **204**, 323–327, DOI: **10.1016/j.matchemphys.2017.10.059**.

31 Z. Zhang, Y. Liu, G. Yao, G. Zu, *et al.*, Synthesis and characterization of $NiFe_2O_4$ nanoparticles via solid–state reaction, *Int. J. Appl. Ceram. Technol.*, 2013, **10**, 142–149, DOI: **10.1111/j.1744-7402.2011.02719.x**.

32 L. Li, J. Chen, Q. Zhang, Z. Yang, *et al.*, Methane dry reforming over activated carbon supported Ni-catalysts prepared by solid phase synthesis, *J. Cleaner Prod.*, 2020, **274**, 122256, DOI: **10.1016/j.jclepro.2020.122256**.

33 P. Rani, J. Thakur, A. Taya and M. K. Kashyap, Magnetocrystalline anisotropy of Pt-doped $L1_0$-FeNi compound for clean energy applications, *Vacuum*, 2019, **159**, 186–190, DOI: **10.1016/j.vacuum.2018.10.023**.

34 L. Chang, C. Wu, Q. Wang, T. Li, *et al.*, Operating interfaces to synthesize $L1_0$-FePt@Bi-rich nanoparticles by modifying the heating process, *Nanoscale*, 2022, **14**, 11738–11744, DOI: **10.1039/d2nr01493a**.

35 L. Lv, J. Liu, J. Zhang, H. Wan, *et al.*, Synergistic regulation of hydrogen adsorption/desorption via dual interfaces of Cu/Ni/$Ni(OH)_2$ toward efficient hydrogen evolution reaction, *Int. J. Hydrogen Energy*, 2022, **47**, 14053–14062, DOI: **10.1016/j.ijhydene.2022.02.156**.

36 Y. Wang, A. Xu, Z. Wang, L. Huang, *et al.*, Enhanced nitrate-to-ammonia activity on copper–nickel alloys via tuning of intermediate adsorption, *J. Am. Chem. Soc.*, 2020, **142**, 5702–5708, DOI: **10.1021/jacs.9b13347**.

37 P. Li, R. Chen, Y. Huang, W. Li, *et al.*, Activating transition metal via synergistic anomalous phase and doping engineering towards enhanced dehydrogenation of ammonia borane, *Appl. Catal., B*, 2022, **300**, 120725, DOI: **10.1016/j.apcatb.2021.120725**.

38 P. Zhang, X. Hui, Y. Nie, R. Wang, *et al.*, New Conceptual Catalyst on Spatial High–Entropy Alloy Heterostructures for High–Performance Li–O_2 Batteries, *Small*, 2023, **19**, 2206742, DOI: **10.1002/smll.202206742**.

39 X. Huang, G. Yang, S. Li, H. Wang, *et al.*, Noble-metal-based high-entropy-alloy nanoparticles for electrocatalysis, *J. Energy Chem.*, 2022, **68**, 721–751, DOI: **10.1016/j.jechem.2021.12.026**.

40 C. Meng, X. Wang, Z. Li, C. Wu, *et al.*, Synthesis of FeCoNiCuPt high-entropy alloy nanoparticles electrocatalysts with various Pt contents by solid-state reaction method, *Mate. Adv.*, 2024, **5**, 719–729, DOI: **10.1039/D3MA00834G**.

41 S. Dong, Z. Li, X. Wang, C. Wu, *et al.*, Optimizing Co content in intermetallic $L1_0$-FeCoPt nanoparticles to enhance the electrocatalytic performance, *J. Alloys Compd.*, 2024, **973**, 172924, DOI: **10.1016/j.jallcom.2023.172924**.

42 B. Qi, W. Chang, Q. Xu, L. Jiang, *et al.*, Regulating Hollow Carbon Cage Supported NiCo Alloy Nanoparticles for Efficient Electrocatalytic Hydrogen Evolution Reaction, *ACS Appl. Mater. Interfaces*, 2023, **15**, 12078–12087, DOI: **10.1021/acsami.3c00385**.

43 X. Zhang, K. Ding, B. Weng, S. Liu, *et al.*, Coral-like carbon-wrapped NiCo alloys derived by emulsion aggregation strategy for efficient oxygen evolution reaction, *J. Colloid Interface Sci.*, 2020, **573**, 96–104, DOI: **10.1016/j.jcis.2020.03.124**.

44 J. Liang, Z. Zhao, N. Li, X. Wang, *et al.*, Biaxial strains mediated oxygen reduction electrocatalysis on fenton reaction resistant $L1_0$-PtZn fuel cell cathode, *Adv. Energy Mater.*, 2020, **10**, 2000179, DOI: **10.1002/aenm.202000179**.

45 H. Jiang, Q. He, X. Li, X. Su, *et al.*, Tracking structural self–reconstruction and identifying true active sites toward cobalt oxychloride precatalyst of oxygen evolution reaction, *Adv. Mater.*, 2019, **31**, 1805127, DOI: **10.1002/adma.201805127**.

46 U.-H. Kim, G.-T. Park, P. Conlin, N. Ashburn, *et al.*, Cation ordered Ni-rich layered cathode for ultra-long battery life, *Energy Environ. Sci.*, 2021, **14**, 1573–1583, DOI: **10.1039/d0ee03774e**.

47 J. Rashid, K. Gilani, A. Arif, C. Saraj, *et al.*, Facile synthesis of NiCo@rGO as bifunctional electrocatalyst for enhanced water splitting, *Int. J. Hydrogen Energy*, 2023, 774–786, DOI: **10.1016/j.ijhydene.2023.07.066**.